Proceedings of ASME Turbo Expo 2011
GT2011
June 6-10, 2011, Vancouver, British Columbia, Canada

GT2011-46037

HP VANE AERODYNAMICS AND HEAT TRANSFER IN THE PRESENCE OF AGGRESSIVE INLET SWIRL

Imran Qureshi[‡*], Andy D. Smith[†], Thomas Povey[‡]

[‡] Department of Engineering Science, University of Oxford, Parks Road, Oxford, OX1 3PJ, UK
[†]Turbine Sub-systems, Rolls-Royce PLC, Moor Lane, Derby, DE24 8BJ, UK

ABSTRACT

Modern lean burn combustors now employ aggressive swirlers to enhance fuel-air mixing and improve flame stability. The flow at combustor exit can therefore have high residual swirl. A good deal of research concerning the flow within the combustor is available in open literature. The impact of swirl on the aerodynamic and heat transfer characteristics of a HP turbine stage is not well understood, however.

A combustor swirl simulator has been designed and commissioned in the Oxford Turbine Research Facility (OTRF), previously located at QinetiQ, Farnborough UK. The swirl simulator is capable of generating an engine-representative combustor exit swirl pattern. At the turbine inlet plane, yaw and pitch angles of over +/-40 degrees have been simulated. The turbine research facility used for the study is an engine scale, short duration, rotating transonic turbine, in which the non-dimensional parameters for aerodynamics and heat transfer are matched to engine conditions. The research turbine was the unshrouded MT1 design.

By design, the centre of the vortex from the swirl simulator can be clocked to any circumferential position with respect to HP vane, and the vortex-to-vane count ratio is 1:2. For the current investigation, the clocking position was such that the vortex centre was aligned with the vane leading edge (every second vane). Both the aligned vane and the adjacent vane were characterised. This paper presents measurements of HP vane surface and endwall heat transfer for the two vane positions. The results are compared with measurements conducted without swirl. The vane surface pressure distributions are also presented. The experimental measurements are compared with full-stage three-dimensional unsteady numerical predictions obtained using the Rolls Royce in-house code Hydra.

The aerodynamic and heat transfer characterisation presented in this paper is the first of its kind, and it is hoped to give some insight into the significant changes in the vane flow and heat transfer that occur in the current generation of low NOx combustors. The findings not only have implications for the vane aerodynamic design, but also for the cooling system design.

Keywords: HP NGV, Heat transfer, Combustor Swirl, Aerothermodynamics, Transonic turbine, Vane, Stator, Turbulence.

1 INTRODUCTION

Highly swirling flows are now widely employed in gas turbine combustors in order to improve the combustion aerodynamics. Swirl enhances the fuel-air mixing and thus reduces peak temperatures, which reduces NOx emissions. In addition, the recirculation zone that develops as a result of strong swirl-induced axial and radial pressure gradients aids flame stability. Significant research is available in the open literature on these topics.

Perhaps because of the rapid development in low-NOx high-swirl combustors, there has been little research that addresses the influence of high residual swirl on the HP turbine. This paper presents the first experimental investigation of the effects of high swirl on HP vane aerodynamics and heat transfer.

2 REVIEW OF PAST LITERATURE

A number of experimental and computational studies have been reported which deal with the effects of swirl on combustion and emission characteristics e.g. [1], [2], [3]. High residual swirl would be expected to influence the flow in the first stage turbine. Most notably, the flow incidence angle to the HP vane, the loading distribution on the HP vane, the inlet velocity profile, the inlet total pressure profile, the free-stream turbulence, the inlet boundary layer profile and the HP

[*] Corresponding author, email: imran.qureshi@eng.ox.ac.uk

secondary flow characteristics would be affected. These changes in turn affect the aerodynamic and heat transfer characteristics, and the performance of a HP turbine. The influence of these parameters on the HP vane has been studied in isolation (mostly in the linear cascade studies), but a comprehensive study incorporating the combined effect of these parameters in a flow representative of a low-NOx combustor has not yet been reported.

Studies relevant to the individual effects, which are combined in the research reported in this paper, are reviewed below.

2.1 Off-Design Incidence and Load Distribution

A number of HP turbine cascade studies have been reported which compare the performance of turbine blades at design and off-design inlet conditions. Jouini et al. [4] investigated the effects of off-design exit Mach number, Reynolds number and inlet flow incidence angle. Significant changes were observed in the loading distribution in the vicinity of the leading edge for off-design incidence angle. For the design exit Mach number, an increase in the losses was observed at off-design incidence angles. Corriveau and Sjolander ([5], [6]) investigated the influence of loading distribution on the performance of HP turbine blades. They observed a reduction of about 20% in the total pressure losses for an aft-loaded airfoil as compared to the baseline airfoil [5].

Weiss and Fottner [7] studied the effects of loading distribution on secondary flows by considering two highly loaded turbine cascades having similar overall loading but different loading distributions. They observed higher secondary loss for the front-loaded cascade. A similar result was observed by Benner et al. [8] who studied the influence of leading-edge geometry on the secondary flow losses and concluded that leading-edge geometry was less significant than loading distribution, which significantly affected the passage vortex and thus the secondary losses.

2.2 Combustor Turbulence and Heat Transfer

Measurements performed at the exit of gas turbine combustors show the turbulence intensity ranges from 15% to 40% [9]. Such high levels of turbulence have a significant effect on the heat transfer to the HP turbine stage. Hancock and Bradshaw [10] and Blair [11] developed correlations for the enhancement of heat transfer as a result of increased freestream turbulence through their studies on flat-plate fully-turbulent boundary layers. Krishnamoorthy and Sukhatme [12] performed experimental investigations using vane/blade cascade geometry and correlated surface heat transfer coefficient enhancement with freestream turbulence for the laminar and turbulent boundary layer regions. Ames et al. [13] measured vane surface heat transfer for different inlet turbulence conditions in a large-scale low-speed linear cascade facility and observed augmentation of heat transfer with high inlet turbulence (dry low NO_x DLN combustor model with Tu ~ 14%) compared to the low inlet turbulence (combustor models with Tu ~ 1%). They also observed early boundary layer transition on the SS with increased turbulence. Similar observations were reported by Radomsky and Thole [14]. Nasir et al. [15] studied the effects of inlet turbulence on vane heat transfer in a transonic cascade facility and also observed augmented heat transfer on both PS and SS of the vane with high freestream turbulence, and earlier transition on the SS. However for exit Mach number of approximately unity, the augmentation on the SS was comparatively small and no effect was observed on the location of boundary layer transition.

2.3 Secondary Flows, Vorticity and Heat Transfer

The fundamental features of secondary flow patterns in NGV passages were proposed by Langston [16] and Sieverding [17], amongst others. This early work was conducted in linear cascades, and although highly significant in establishing the basic mechanisms that apply in all cascades (both linear and annular) it is now acknowledged that the flow pattern in the annular cascade is very different from the linear counterpart. For this reason there is now more emphasis on the annular experiment, or the full rotating turbine experiment, where there is a desire to accurately understand the extent of secondary flow vortices generated in a modern gas turbine engine, and the impact of these secondary flows on loss. Annular cascades tend to have more restricted regions of secondary flow, with less cross-passage flow than suggested by studies in linear cascades. In both linear and annular cascades, the generation of secondary flow vortices has been found to affect the local heat transfer characteristics on the endwalls, and on the vane SS near the endwalls.

In the situation where the combustor exit flow has residual swirling motion, the flow at the inlet to the turbine stage will have additional vorticity. This vorticity is propagated through the turbine stage which accordingly changes the aerodynamic and heat transfer characteristics. It is expected that the additional vorticity will increase the mixing of boundary layer and freestream fluid which will lead to an enhancement in heat transfer.

The generation of vortices is encouraged in heat exchangers for this reason: the vortices having the effect of promoting mixing and therefore thinning of the boundary layer. Yilmaz et al. [18] observed an augmentation of up to 98% in Nusselt number in their swirling flows experiments compared to the baseline no-swirl flow. Jacobi and Shah [19] reviewed studies of heat transfer enhancement using longitudinal vortices. The overall (averaged) heat transfer enhancement observed in the studies reviewed ranged up to 100% with local heat transfer enhancement up to 200% in some cases.

3 EXPERIMENTAL FACILITY

The Oxford Turbine Research Facility (OTRF), previously called Turbine Test Facility (TTF) when sited at QinetiQ Farnborough, is a short duration transonic light-piston facility. It can be operated as a single or 1.5 stage turbine, and for the current study was operated with the full-scale MT1 research turbine. The main components of the facility are: i) the high pressure reservoir; ii) the pump-tube that contains a light-weight piston; iii) a fast acting plug valve; iv) the turbine stage (working section); v) the turbobrake. These are highlighted in the schematic of the research facility shown Figure 1.

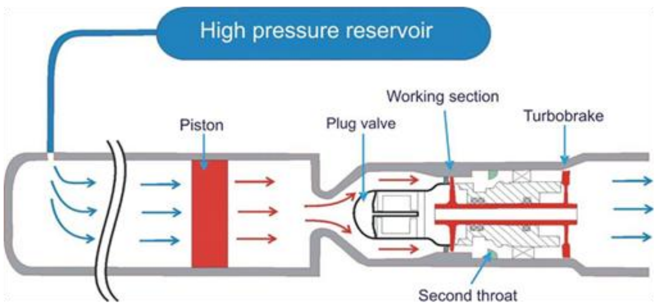

Figure 1: Schematic of the Oxford Turbine Research Facility.

The operating principles of this type of facility were first described by Jones et al. [20]. Prior to an experimental run the plug valve is closed, the working section and exhaust tank are evacuated, and the turbine disc is accelerated to the design speed using an air motor. Air from the high pressure reservoir is then injected into the piston tube behind the light piston. The piston moves down the piston tube acting to compress and heat the air in front of it (approximately) isentropically. When the desired test gas conditions (of pressure and temperature) are achieved in this compression, the fast-acting plug valve is opened and the test gas (air) flows out of the piston tube into the large annulus. Here the gas settles in an annulus which is similar to combustor geometry, before passing through the working section. The test run ends when the piston reaches the end of the piston tube, at which point the test gas has been processed by the turbine. Steady conditions are achieved for approximately 500 ms, during which the experimental data are acquired. During the test period all relevant non-dimensional parameters are matched to engine conditions. The turbobrake [21] ensures approximately constant turbine speed during the run. The OTRF has been used to test a number of HP turbine stages [22] and a number of 1.5 stage turbines [23] in the past.

The nominal operating conditions of the research facility for the MT1 turbine stage, used in the current study, are listed in Table 1.

The working section of the OTRF is shown in Figure 2. The MT1 research turbine has 32 NGVs and 60 rotor blades. The NGV true chord and the exit swirl angle are 70.1 mm and 74.4º at the mid-span location. The vane has an aspect ratio of 0.53 and an exit Reynolds number of 2.6 x 10^6. For the current investigation, the research facility was upgraded with the installation of an inlet swirl generator. This is briefly described in the next section.

Table 1: MT1 turbine stage operating conditions.

Parameter(unit)	*Nominal value*	*Allowable run-to-run variations around nominal value (%)*
p_{01} (bar)	4.6	± 1
T_{01} (K)	444	± 2
T_g/T_w	1.50	± 2
M_2^{hub}	1.054	± 1
M_2^{casing}	0.912	± 1
ω (rpm)	9500	± 1
p_{02rel} (bar)	2.697	± 1

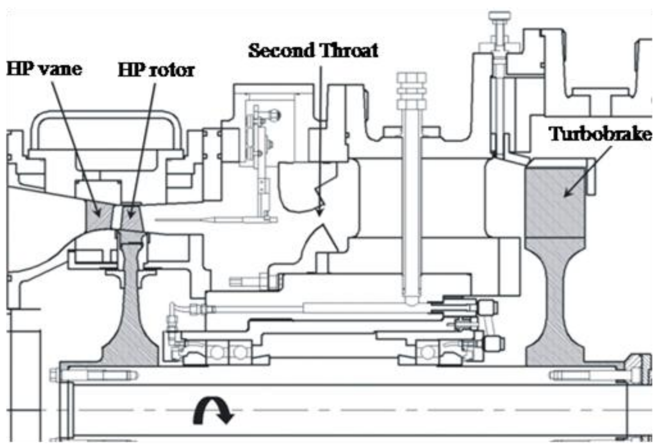

Figure 2: The working section of the OTRF with the HP turbine stage and turbobrake highlighted.

4 INLET SWIRL SIMULATOR

In order to carry out detailed experimental investigations of the effects of swirl on the HP turbine stage, an inlet swirl simulator has been designed and commissioned in the Oxford Turbine Research Facility (OTRF). The target swirl profile at the turbine stage inlet was based upon extreme exit swirl conditions for a low-NO_x modern combustor. Peak yaw and pitch angles were over +/-40 degrees. The development, installation and commissioning of the swirl simulator in the OTRF is discussed by Qureshi and Povey [24].

The swirl simulator module is designed to mount in the tunnel flow path upstream of the OTRF inlet contraction. The module allows rotation so that clocking of the vortex core with respect to the NGV leading edge could be achieved. To aid in CFD comparison, and to allow repeatability assessment around the annulus, an integer swirler-to-vane count ratio of 1:2 was chosen (16 swirlers and 32 NGVs). The manufactured swirl generation system (approximately 1 m diameter), is shown in Figure 3. Each swirler is composed of six flat-plate vanes inclined at 40º to the axial direction (swirl number = 0.7). The flow conditions measured at the inlet to the HP turbine with inlet swirl are presented in section 5.

Figure 3: The assembled inlet swirl simulator module.

5 INLET CONDITIONS WITH SWIRL

Swirl profile measurements were performed using the rakes of four-hole probes at about 0.7 axial chords upstream of the vane inlet plane. Details of the necessarily unconventional four-hole probes arrangements are discussed in [24]. Area survey was conducted over one swirler pitch (or 2 NGV pitches). The results for the measured pitch angle (β) and the yaw angle (α) are presented in Figure 4 and Figure 5 respectively.

The circular dots indicate the points at which pitch and yaw measurements were possible. Because of the high compound swirl angles, at some points it was not possible to reduce the data using the calibration maps.

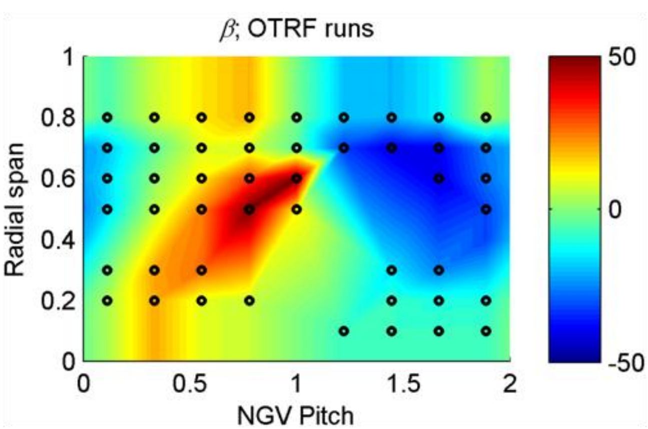

Figure 4: Pitch angle profile measured 0.7 C_{ax} upstream of NGV inlet plane with inlet swirl.

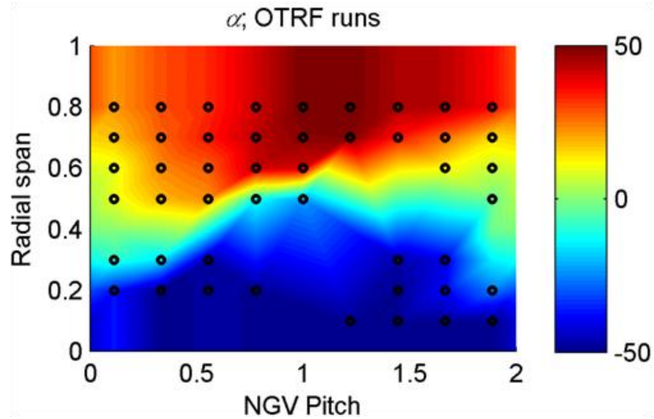

Figure 5: Yaw angle profile measured 0.7 C_{ax} upstream of NGV inlet plane with inlet swirl.

These regions have been filled with the results at the nearest measured locations in the area plots. The profiles of pitch and yaw angle correspond to a well defined clockwise vortex (as viewed from upstream) of approximately the desired target magnitude. The corresponding flow vectors are presented in Figure 6. The thick arrows represent locations where a measurement was possible. Points based on interpolated/extrapolated data are marked as thin arrows.

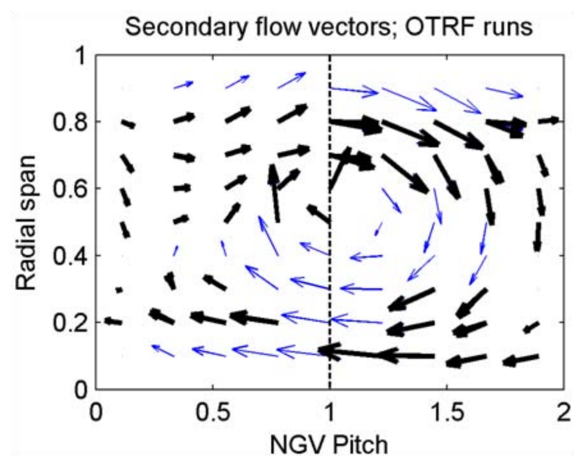

Figure 6: Measured inlet secondary flow vectors (bold arrows) and interpolated/extrapolated vectors (thin arrows).

The yaw angle profile measured in the OTRF is compared with the target profile in Figure 7. Results are presented at 20% and 80% span. The measured peak yaw magnitude (approximately 50 degrees) is well over the target value indicating a well-formed clockwise vortex as desired.

The inlet total pressure profile was also determined using the four-hole probe data. The measured non-dimensional pressure profile is presented in Figure 8. For the uniform inlet condition, the total pressure variation from the nominal mass-mean value at the inlet plane was approximately +/- 0.3%. With inlet swirl a variation of +/- 1.5% from the nominal mass-mean value of total pressure was observed.

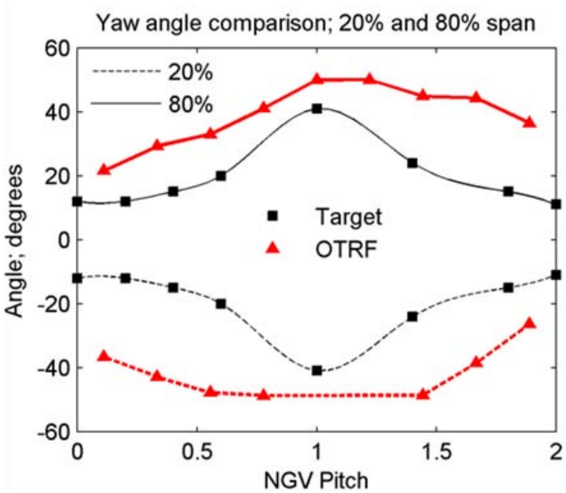

Figure 7: Yaw angle profile at 20% and 80% span; comparison of measurements in the OTRF with the target profile.

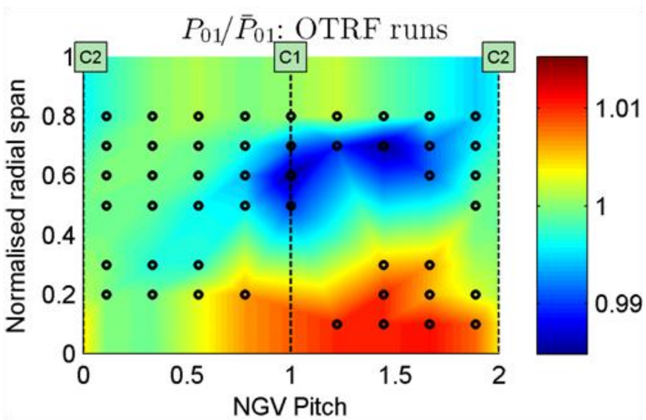

Figure 8: Normalised inlet total pressure profile with swirl.

The notation C1 and C2 is used to refer to leading edge point aligned with the vortex centre (C1) and the leading edge between vortices (C2). This is illustrated in Figure 9. The notation is also used to refer to the vanes similarly disposed with respect to the vortex.

An inlet total temperature survey was also performed with inlet swirl. No significant variation from the nominal uniform inlet temperature condition was observed.

6 EXPERIMENTAL INSTRUMENTATION AND DATA REDUCTION

Experimental pressure and heat transfer measurements were conducted on the HP vane surface and the endwall. A brief description of the instrumentation and data processing is given below.

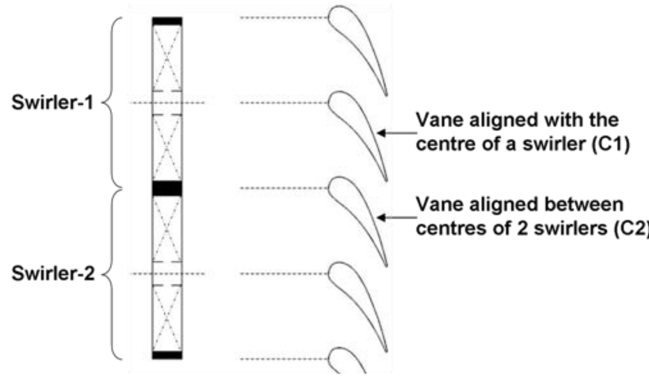

Figure 9: Schematic to show notation used to refer to HP vane geometric alignment with respect to the vortex centre.

6.1 NGV Pressure Measurements

The HP vane static pressure distributions were measured at 10, 50 and 90% span with and without inlet swirl. Pneumatic tappings were distributed over a set of vanes to achieve a good resolution of data at each span location. Instrumented vanes were assembled in a removable cassette.

6.2 NGV Heat Transfer Measurements

Heat transfer measurements were performed at 10, 50 and 90% spans on the SS and PS of the HP NGV. Measurements were obtained with and without inlet swirl. Thin-film platinum-resistance gauges (0.2x2 mm in size) were used. A two-layered substrate was used: an insulating layer of Kapton™ (polyamide) on a (thermally) semi-infinite layer of metal. The theory for the use of multi-layered gauges is given in Doorly and Oldfield [25].

For the uniform inlet condition, one vane was instrumented for each of PS and SS at each span location. However for inlet swirl, 2 vanes (labelled n1 and n2) were instrumented for each of PS and SS at each span-wise location. The heat flux was evaluated from the measured surface temperature time history using the Impulse Response Method, as described by Oldfield [26]. The heat flux data was reduced to Nusselt number using the vane inlet total temperature and the vane true chord as given by Eq. (1). The thermal conductivity was evaluated at the inlet total temperature.

$$Nu_{T01} = \frac{\dot{q}C}{(T_{01} - T_w)k_{T01}} \tag{1}$$

6.3 Endwall Heat Transfer Measurements

Heat transfer measurements were obtained on the vane hub and casing endwalls using approximately 50 thin-film platinum-resistance gauges on a Macor™ (machineable glass) single layer substrate. Heat transfer electrical analogue (HTA) circuits [27] were used to convert measured resistance (surface temperature) into heat flux.

Using the measured heat flux data, the temperature history was reconstructed for each gauge as described in Oldfield et al. [28]. During a run, the heat flux drops with time as the surface temperature rises. By extrapolated regression of heat flux against reconstructed temperature the local adiabatic wall temperature at each gauge location was obtained [28]. Nusselt number, based upon the vane true chord, was obtained using the relation given in Eq. (2). The thermal conductivity of air was evaluated at mean inlet total temperature.

$$Nu = \frac{\dot{q}C}{(T_{aw} - T_w)k_{T01}} \tag{2}$$

Although the endwall heat transfer measurements with inlet swirl were not within the scope of the present programme, the measurements with uniform inlet temperature are presented for CFD validation, followed by a discussion of the CFD predicted changes in heat transfer with inlet swirl.

6.4 Measurement Uncertainty

A detailed treatment of uncertainty in the heat transfer measurement process in the transient turbine experimental environment is provided by Povey [29]. Estimated precision and absolute uncertainties for uniform inlet conditions and for inlet swirl are presented in Table 2 below.

Table 2: Estimated precision and absolute uncertainty in measured and derived variables

Variable	*Precision*		*Absolute Uncertainty*	
	Uniform	Swirl	Uniform	Swirl
T_{01}	± 1 K	± 3 K	± 5 K	± 7 K
T_w	± 1.5 K	± 1.5 K	± 1.5 K	± 1.5 K
$\dot{q}$	1.5%	1.5%	3.4%	3.4%
T_{aw}	± 1 K	± 3 K	± 5 K	± 7 K
Nu	1.9%	3.6%	5.6%	7.6%

7 NUMERICAL SIMULATIONS

Three-dimensional computational simulations were conducted with and without inlet swirl and the predictions were compared with experimental results. The measured values of pitch and yaw (Figure 4 and Figure 5) were used as inlet boundary conditions for the swirl simulations. Uniform total pressure fields were used for both the uniform simulation and that with inlet swirl, and this must be considered when interpreting results (see measured profile – Figure 8).

The swirler-to-vane count ratio was 1:2, so a structured computational grid comprising 2 NGVs and 4 rotor blades (actual vane/blade count is 32/60), was developed using Rolls-Royce in-house tool PADRAM, having over 5 million mesh cells. The rotor airfoils were skewed by a small angle to reproduce the rotor capacity of the original geometry. The computational solutions were obtained using the Rolls-Royce in-house CFD solver HYDRA, which uses an efficient edge-based data structure, as described by Moinier and Giles [30]. A MUSCL based flux-differencing algorithm is used to integrate the flow equations around median-dual control volumes. Block Jacobi pre-conditioning of the discrete flow equations is applied [31] and a 5-stage Runge-Kutta scheme is employed for convergence of the steady state solution [32]. An element-collapsing multi-grid algorithm is used to accelerate the convergence to steady state [33]. Nonlinear unsteady calculations were performed using implicit dual time-stepping.

Both steady and unsteady solutions were obtained. The results from unsteady solutions were time-averaged for comparison with steady solutions. The Spalart-Allmaras turbulence model was implemented with wall functions. The boundary layers were modelled as turbulent. For each case, two solutions were obtained at two isothermal wall temperatures, T_{w1} and T_{w2}, allowing the heat transfer coefficient to be determined from the heat fluxes using Eq. (3). Adiabatic wall temperature was obtained by substituting heat transfer coefficient in either Eq. (4) or Eq. (5). The Nusselt number was obtained using Eq. (2).

$$h = \frac{(\dot{q}_1 - \dot{q}_2)}{(T_{w2} - T_{w1})} \tag{3}$$

$$\dot{q}_1 = h(T_{aw} - T_{w1}) \tag{4}$$

$$\dot{q}_2 = h(T_{aw} - T_{w2}) \tag{5}$$

8 RESULTS AND DISCUSSION

Experimental measurements and computational predictions of pressure and heat transfer on the NGV and platform surfaces are now presented and discussed.

8.1 NGV Isentropic Mach number

The presence of intense swirl in the flow significantly alters the incidence angle at the inlet of HP vane. The predicted difference in incidence at a plane, 0.25 axial chords upstream of the vane leading edge, between the case of inlet swirl and uniform conditions is shown in Figure 10. The positions of the vane leading edges C1 and C2 are marked.

Vane C1 is downstream of the vortex core, and is subject to the largest change in incidence: approximately -50º at the casing and +50º at the hub. Between vortex cores, in position C2, the general positive circulation of flow near the casing, and negative circulation of the flow at the hub is still evident, though less pronounced. Here the incidence is approximately -30º at the casing and +20º at the hub. Near the mid-span on both vane C1 and C2 there is a small region of approximately nominal flow angle (0º), but the flow-field is otherwise dominated by high whirl angles.

The incidence angle difference causes a significant change in the position of the stagnation line on the vane leading edge.

The shift in the stagnation point near the hub and the casing is shown using predicted streamlines in Figure 11.

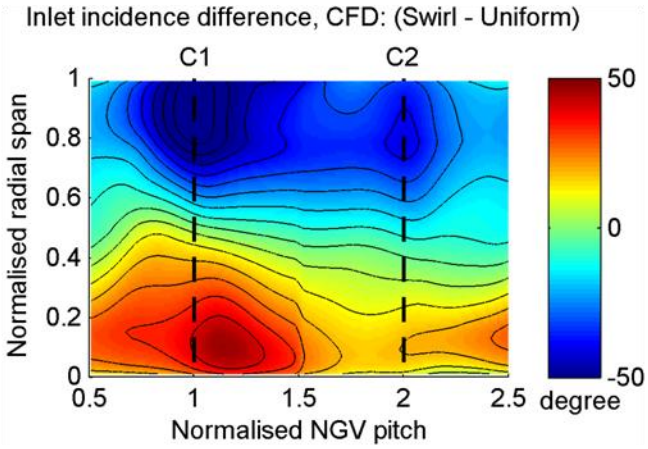

Figure 10: Predicted difference of inlet incidence angle with inlet swirl; 0.25 axial chords upstream of the vane leading edge.

For vane C1, the stagnation point with inlet swirl moves towards the PS near the hub, and towards the SS near the casing. The effect is pronounced, and sufficient to cause a change in the loading of the vane, the heat transfer and the loss. This is discussed subsequently.

On vane C2 a similar shift of the stagnation line is observed, though less pronounced at the casing (compared to C1) and close to negligible near the hub.

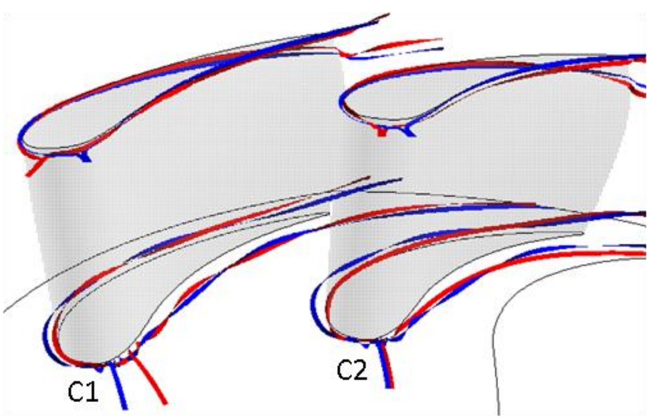

Figure 11: Predicted streamlines for uniform flow (blue) and flow with inlet swirl (red), showing shift of the stagnation line.

The change in flow incidence affects the loading distribution of the airfoil. The measured HP NGV isentropic Mach number distributions at 10, 50 and 90% span with inlet swirl are presented in Figure 12, Figure 13 and Figure 14 respectively, for vane C1. Results obtained with uniform inlet conditions are plotted for comparison. The time-averaged unsteady CFD predictions are also presented for comparison.

There is a significant increase in measured aerodynamic loading at 10% span, associated with the high positive incidence near the hub section of the vane. This is confined to the region of about 0-40% axial chord on the suction surface, but is evident along the entire pressure surface.

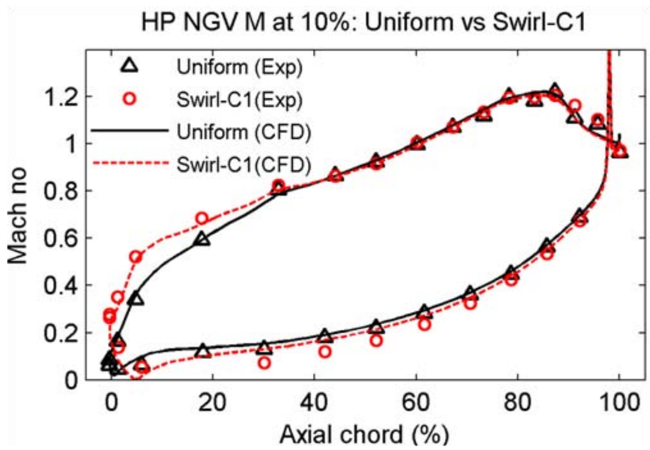

Figure 12: NGV isentropic Mach number at 10% span for uniform inlet conditions and inlet swirl for position C1; comparison of measurements and CFD.

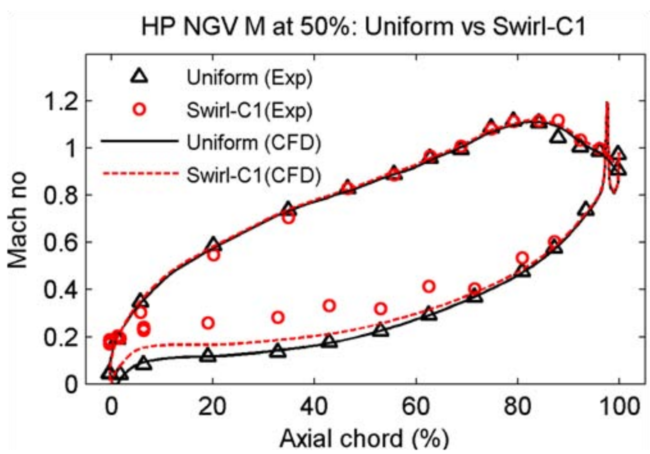

Figure 13: NGV isentropic Mach number at 50% span for uniform inlet conditions and inlet swirl for position C1; comparison of measurements and CFD.

At 50% span, a reduction in the measured loading was observed, caused by an increase in the pressure surface Mach number. At 50% span the SS isentropic Mach number was not significantly affected. The apparent change in PS isentropic Mach number may be an artefact of the low total pressure vortex core being ingested predominantly on the PS of vane C1. At 30% axial chord, a change from approximately M = 0.15 to M = 0.25 would be consistent with a change in total pressure of -2.7%. Figure 8 reveals a deficit in total pressure of approximately 1.5%, which is the correct order of magnitude. This argument is also consistent with the disappearance of a stagnation region in the leading part of the vane when presented in terms of isentropic Mach number.

At 90% span, there is a decrease in loading with inlet swirl associated with high negative incidence in this region. This causes a region of negative pressure gradient on the PS of the vane between approximately 5% and 30% span.

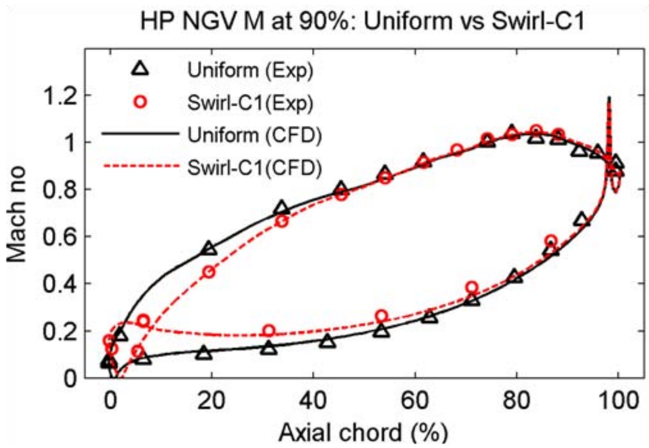

Figure 14: NGV isentropic Mach number at 90% span for uniform inlet conditions and inlet swirl for position C1; comparison of measurements and CFD.

The computational predictions were generally in very good agreement with the measurements on all the surfaces at each span with the exception of 50%-PS (significant difference) and 10%-PS (small difference). Here the change in isentropic Mach number with inlet swirl was lower (50%-PS) or higher (10%-PS) in the prediction than in the experimental case. This is likely due to the approximation of uniform inlet total pressure in the computations. In the experiment, vane C1 is subject to higher than average total pressure in a region near the PS at 10% span, and lower than average total pressure in a region near the PS at 50% span. These non-uniformities would act to lower the inferred isentropic Mach number in the experiment at 10% span and increase it at 50% span, which is consistent with the measurements. It is noted that the predictions are in excellent agreement for all span locations for position C2 (presented below), where the non-uniformity in total pressure is lower.

The measured HP NGV isentropic Mach number distributions with and without inlet swirl at 10, 50 and 90% span for vane C2 are presented in Figure 15, Figure 16 and Figure 17 respectively. The general trends with inlet swirl are similar to those observed for vane C1, but the change with swirl is less significant. This is expected when the whirl distribution is considered.

At 10% span, a small increase in loading was measured, which is in-line with the small change in incidence expected, and observed in the CFD solutions. The decrease in loading at 50% was also relatively small.

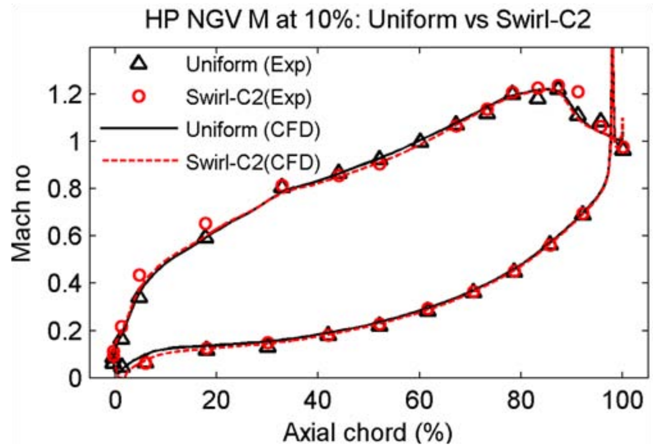

Figure 15: NGV isentropic Mach number at 10% span for uniform inlet conditions and inlet swirl for position C2; comparison of measurements and CFD.

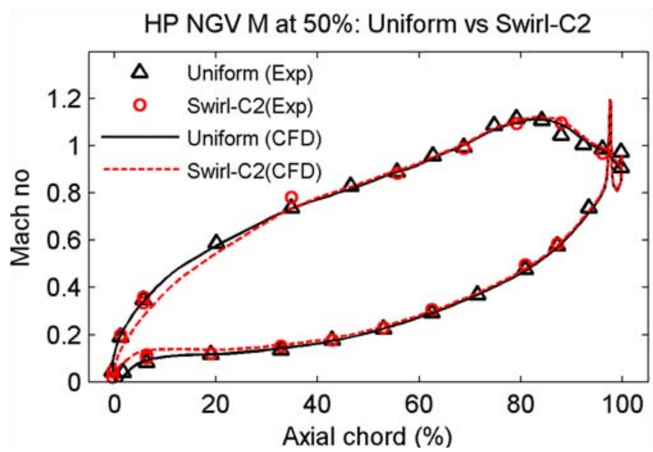

Figure 16: NGV isentropic Mach number at 50% span for uniform inlet conditions and inlet swirl for position C2; comparison of measurements and CFD.

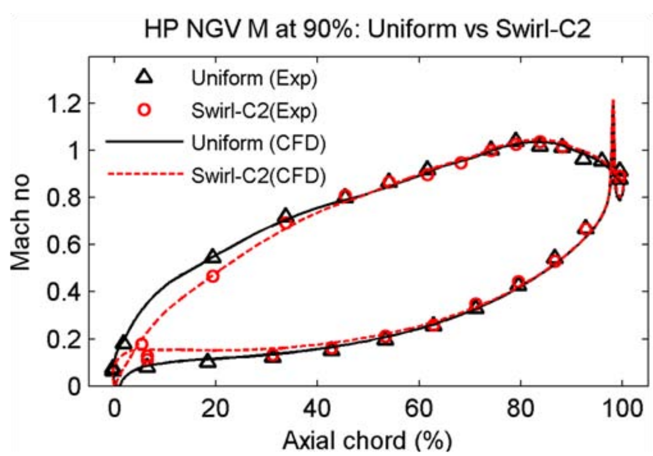

Figure 17: NGV isentropic Mach number at 90% span for uniform inlet conditions and inlet swirl for position C2; comparison of measurements and CFD.

At 90% span where the expected incidence difference was highest, measurements show a significant reduction in loading (though less than for vane C1) in the region 0-50% axial chord. There is a region of mild negative pressure between 5% and 30% axial chord on the PS.

The agreement between CFD and experiment is good at all span heights on both the PS and SS of the vane. Figure 8 reveals relatively uniform total pressure at inlet to the vane for position C2, making the approximation in the computational boundary conditions more sound at this location.

The measured changes in aerodynamic loading would cause a change in loss characteristics of the vane. This is examined with reference to the computational results. The area plots of the difference in total pressure loss coefficient (where C_{PL} is computed using Eq. (6)) evaluated at the vane exit plane, between the swirl inlet condition and uniform inlet condition are presented in Figure 18 (C1) and Figure 20 (C2). Results are presented viewed from upstream to downstream.

$$C_{PL} = \frac{(P_{01} - P_{02})}{(0.5\rho u^2)|_{02}} \tag{6}$$

Consider the change in total pressure loss with inlet swirl for vane C1, presented in Figure 18. In the hub region there are two additional loss cores (a) and (b) on the suction side of the vane. Loss core (a) is close to the vane surface at approximately 15% span. Examination of the surface streamlines presented in Figure 29 shows that there is significant downwash of flow on the SS with inlet swirl, causing the boundary layer fluid to collect at approximately 15 span. This is matched by divergence of streamlines for flow arriving in the 20% to 60% span region at the trailing edge (TE). This spreading of boundary layer fluid accounts for the deficit in loss in this region (d). The second loss core (b) suggests enhanced secondary flow caused by the higher loading in the hub region. Higher loading leads to higher surface velocities over the majority of the vane SS, and also higher boundary layer loss. On the PS of the vane there is a region of lower loss (c). This is in the boundary layer region, and is likely the result of lower surface velocities on the PS at 10% span, resulting from high positive incidence. With reference to Figure 29, it is clear that the PS streamline pattern for vane C1 has strong divergence of streamlines (compared with the uniform inlet case) which leads to redistribution of loss from the hub region (c) to the casing region where there is enhanced total pressure loss in the whole of the boundary layer region (f). The enhanced loss (f) is likely exacerbated by increased velocities and possible separation of the PS boundary layer at the 90% span section (see Figure 14). Close to 90% span SS there is a region of significant loss reduction (e) which appears to be associated with lower surface velocities (see Figure 14) and streamline divergence (see Figure 29). The features (g) and (h) appear to be weakened and strengthened corner vortices, respectively.

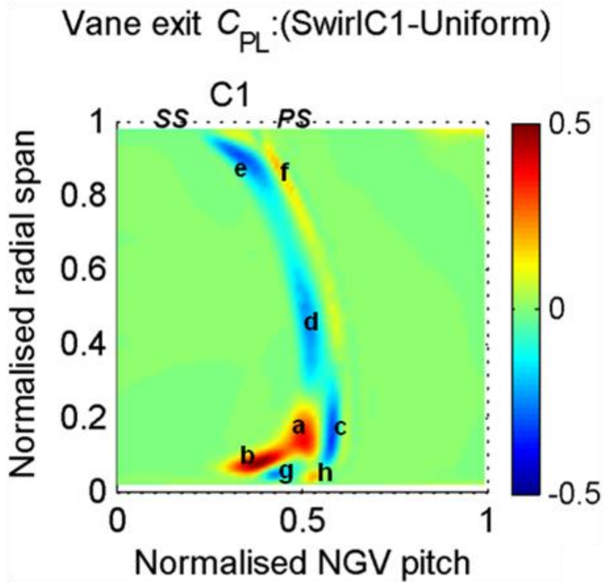

Figure 18: Predicted pressure loss coefficient difference at vane exit between swirl and uniform conditions; position C1.

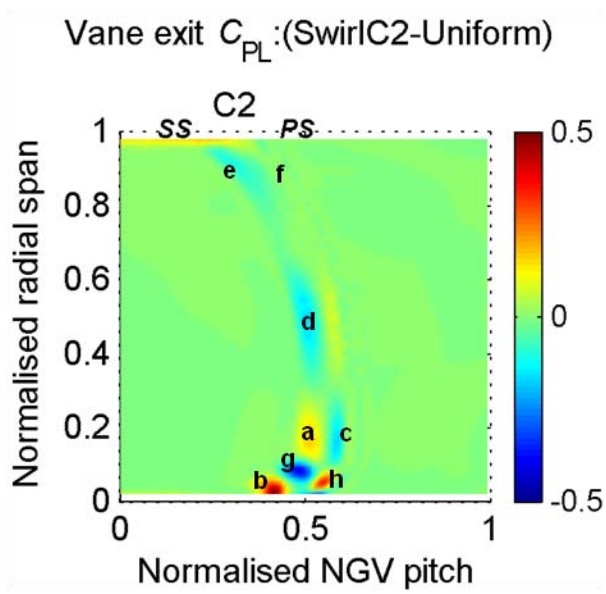

Figure 19: Predicted pressure loss coefficient difference at vane exit between swirl and uniform conditions; position C2.

Consider the change in total pressure loss with inlet swirl for vane C2, presented in Figure 19. The general picture is similar to vane C1, but with reduced magnitude of most of the features. This is in accord with general trends in Figure 15 to Figure 17, and the streamline pattern in Figure 29.

Loss core (a) is less enhanced than was the case for position C1, which is explained by the streamline pattern (Figure 29) which shows less accumulation of SS boundary layer fluid in this region for position C2. The weakening of the loss regions (d) and (e) on the SS are less pronounced for C2 than for C1, which is in line with the reduced change in vane loading. Likewise the PS boundary layer loss band (f) is less enhanced than for position C1, which is the result of less lateral redistribution of loss on the PS (Figure 29) and a reduction in the increase in surface velocity (Figure 17) compared with the C1 position (Figure 13). In the hub region on the SS, the enhancement in loss core (b) is less than for position C1, and the vortex is pushed closer to the endwall. This leads to an area of reduced loss (g) which marks the position the vortex adopted in the uniform inlet flow case.

A comparison of the circumferentially-averaged pressure loss coefficient at vane exit is presented in Figure 20 for the uniform situation, and for vanes with inlet swirl in position C1 and C2.

For C1 an increase in loss is observed in the hub region which extends to approximately 25% span. The peak at 10% span is associated with the displaced passage vortex (b), and the increase between 10% and 25% span is associated with the redistribution of the boundary layer loss from the casing to the hub region. This is manifested as loss region (a) in Figure 18. From 25% to 90% span loss is reduced. This is caused by the redistribution of boundary layer fluid to the hub region and the decreased loading of the vane in the casing region. The overall difference in loss between C2 and the uniform case is less striking than for C1.

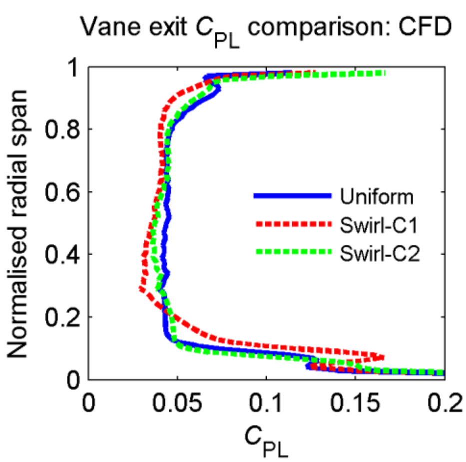

Figure 20: Predicted radial pressure loss coefficient distributions downstream of NGV for uniform inlet conditions and for inlet swirl in positions C1 and C2.

8.2 NGV Surface Heat Transfer Results

With inlet swirl, the NGV surface heat transfer is affected by increased inlet turbulence (compared to the uniform condition), changes in the secondary flow pattern, and changes in vane loading.

The measured freestream turbulence intensity at the turbine inlet plane in the OTRF for uniform inlet flow was found to be 6.5% (Chana, [34]). Beard [35] measured the turbulence intensity with inlet swirl as 11.2%. The impact on heat transfer coefficient of increased inlet turbulence was estimated using the correlation given in Eq. (7) (see [12]). Using this, an increase in *h* of 11% was estimated.

$$h_x = h_{(Tu=0)}(1+0.0235Tu_x) \qquad (7)$$

Although this is significant, it might be expected that larger changes would arise because of gross changes in the flow structure within the passage. Figure 21 shows the predicted streamlines for the uniform case, obtained by tracking particles marked at the vane inlet plane, at the 10, 50 and 90% span locations (where the heat transfer measurements have been performed). For the uniform inlet condition there is little radial movement of the streamlines, demonstrating the relatively low secondary flow within the passage.

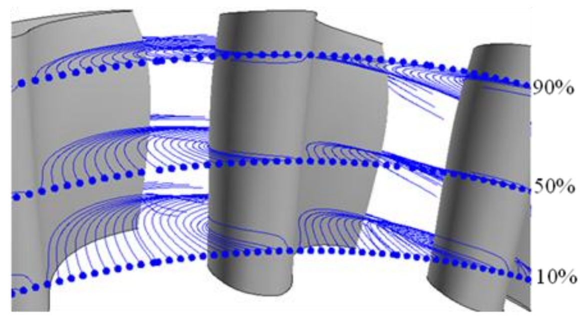

Figure 21: Predicted passage streamlines at 10, 50 and 90% span for uniform inlet conditions.

For inlet swirl, there is significant radial movement of streamlines as shown in Figure 22, Figure 23 and Figure 24 for 90, 50 and 10% span respectively.

At 90% span the effect of the clockwise inlet swirl vortex is significant, causing significant upwash on the PS of vane C1. At this span, the SS of vane C1 and the PS and SS of vane C2 are less affected.

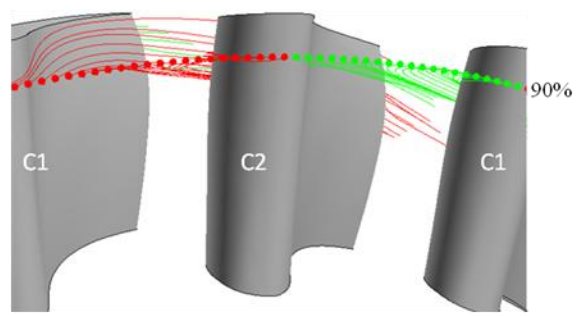

Figure 22: Predicted passage streamlines at 90%, span for inlet swirl.

At 50% span the effect of swirl is most pronounced. There is significant upwash on the PS of vane C1, and downwash on the SS of vane C2, consistent with an additional vortex in the passage bounded (from L to R) by C1-C2. The same effect is observed in the passage bounded (from L to R) by C2-C1, but it is less pronounced.

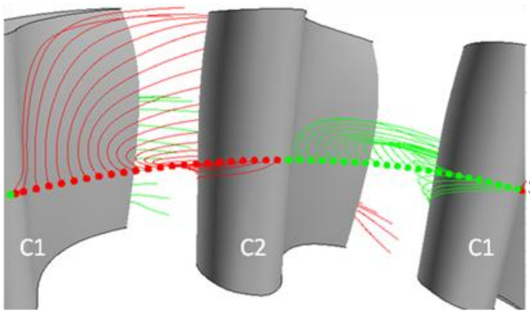

Figure 23: Predicted passage streamlines at 50%, span for inlet swirl.

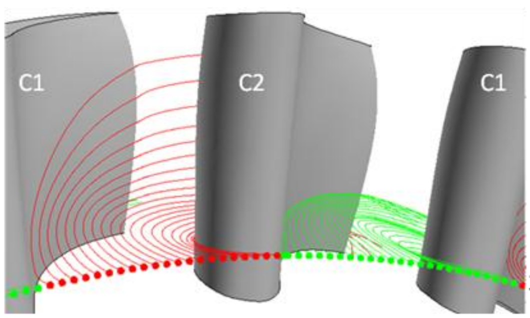

Figure 24: Predicted passage streamlines at 10%, span for inlet swirl.

At 10% span in passage C1-C2 there is significant upwash on the PS of vane C1, and mild downwash on the SS of vane C2. The flow in passage C2-C1 is comparatively less affected by inlet swirl.

Computational results of secondary flow velocity components can be helpful in visualising the flow field. In Figure 25 to Figure 28 the difference between the secondary flow velocity vectors for the uniform and swirl cases are presented.

Figure 25 presents the difference in the secondary flow vectors at 0.25 axial chords upstream of the NGV inlet. Two clockwise vortices, generated by two neighbouring upstream swirlers are aligned with the leading edge of vanes in position C1. The vane in position C2 is approximately aligned with the middle of these vortices as expected.

At the vane inlet plane (Figure 26), the vortex is divided by vane C1, resulting in a clockwise vortex within the passage (from L to R) C1-C2. This causes upwash on the PS of vane C1 and downwash on the SS of vane C2. In passage C2-C1 (from L to R) the effect is less pronounced, with the vortex being restricted to the right hand side (RHS) of the passage, near the SS of vane C1.

Figure 27 shows the difference in secondary flow vectors 0.25 axial chords downstream of the vane inlet plane. In passage C1-C2 the vortex has become more regular and filled the passage, causing, in particular, significant upwash on the PS of vane C1. At the same axial station, the vortex on the RHS of passage C2-C1 remains confined to this region of the passage.

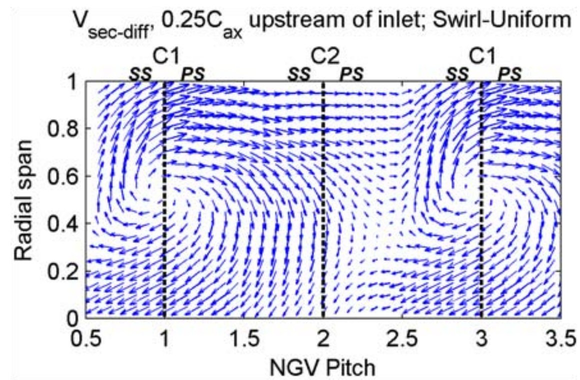

Figure 25: Difference of secondary flow velocity vectors between swirl and uniform; $0.25C_{ax}$ upstream of inlet.

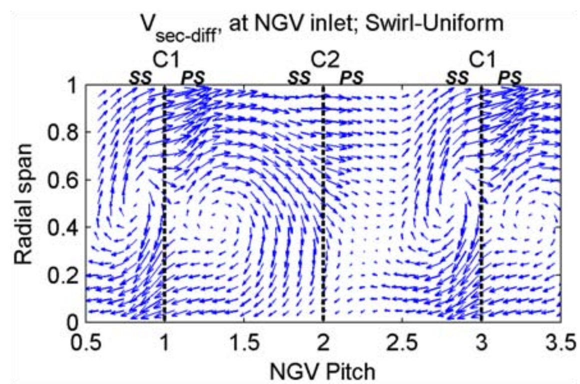

Figure 26: Difference of secondary flow velocity vectors between swirl and uniform; at NGV inlet plane.

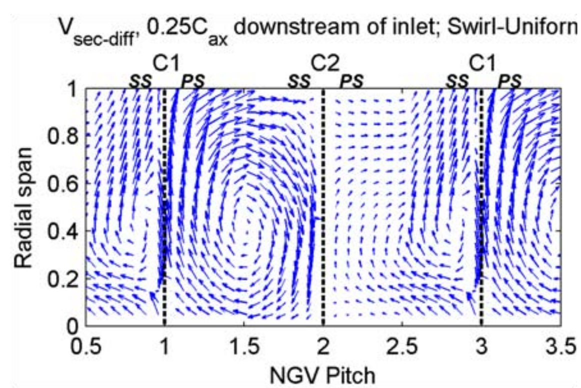

Figure 27: Difference of secondary flow velocity vectors between swirl and uniform; $0.25C_{ax}$ downstream of inlet.

At the vane exit plane the vortex structure is weakened, but there is still evidence of upwash on the PS of vane C1.

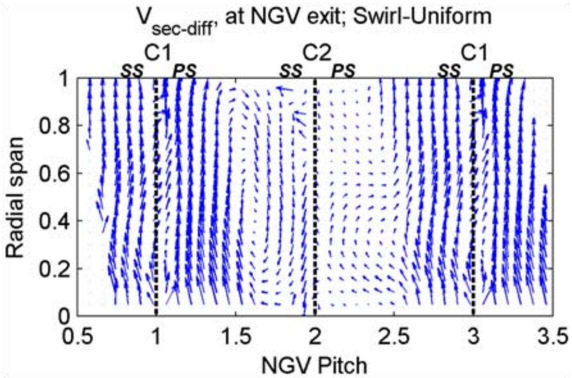

Figure 28: Difference of secondary flow velocity vectors between swirl and uniform; at NGV exit plane.

The impact of these vortices on the NGV surface streamline pattern is shown in Figure 29. The streamline pattern is significantly altered by inlet swirl. Of particular note is the extreme upwash on the PS of vane C1, which causes boundary layer fluid to accumulate at the 90% span location. This causes a region of increased loss (f) illustrated in Figure 18. The strong downwash on the SS of vane C1 causes boundary layer fluid to accumulate at approximately 15% span, which is manifested in loss core (a) in Figure 18. Where there is streamline divergence there is a thinning of the boundary layer, and lower loss. It is expected that the heat transfer will follow and inverse relationship, being low where there is accumulation of boundary layer fluid and high where there is thinning of boundary layer fluid.

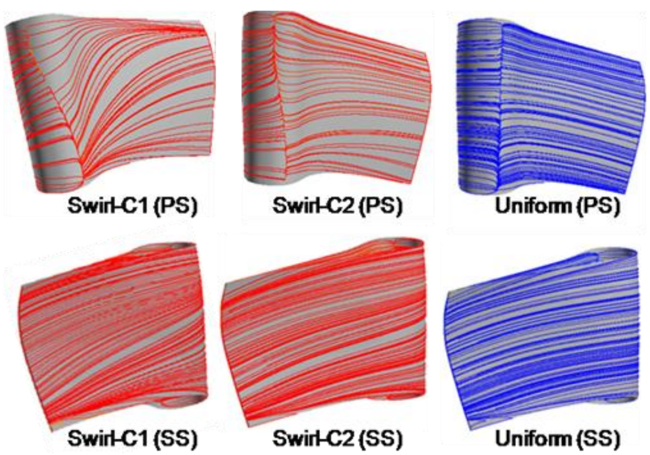

Figure 29: Predicted NGV surface flow streamlines, with and without inlet swirl.

HP NGV surface heat flux was measured with uniform inlet conditions and with inlet swirl, and reduced to Nusselt number as described in section 6.2. At each vane location (C1 and C2) a set of two different vanes was instrumented so that repeatability comparisons could be performed. These vanes are termed as n1 and n2 for each surface-span in the following plots.

The results for inlet swirl for the NGV in position C1 are compared to the uniform inlet data in Figure 30, Figure 31 and Figure 32 for 10, 50 and 90% span respectively.

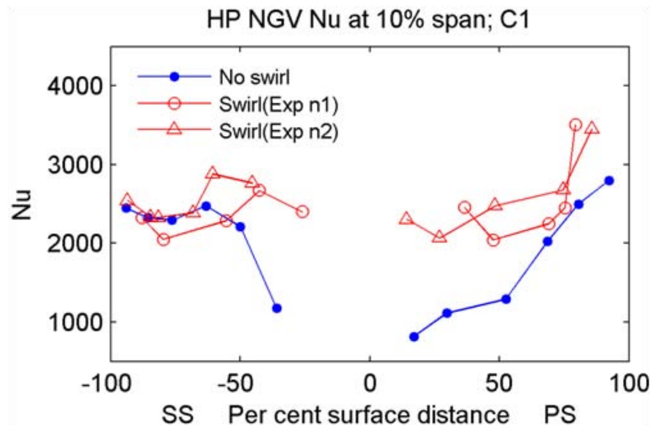

Figure 30: NGV Nu at 10% span; Uniform and Swirl-C1.

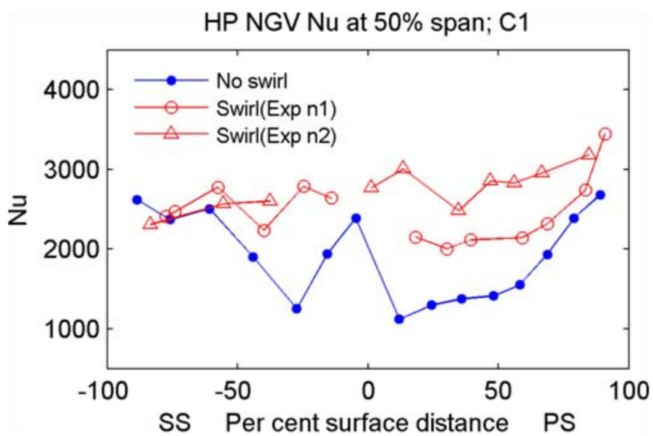

Figure 31: NGV Nu at 50% span; Uniform and Swirl-C1.

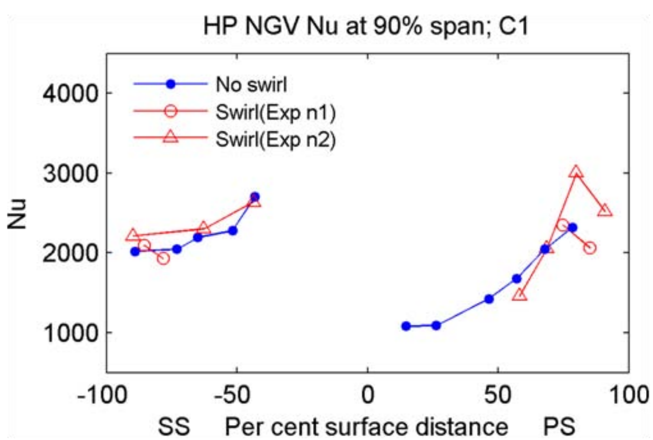

Figure 32: NGV Nu at 90% span; Uniform and Swirl-C1.

At 10% span an increase in Nu is observed over most of the chord. On the PS of the vane the enhancement is significant, being greatest on the leading part of the vane. This is a region of strongly diverging boundary layer fluid (see Figure 29) in which thinning is expected. Higher loading will also tend to increase surface heat transfer coefficient, as observed – less significantly – on the SS of the vane. It is noted that the SS Nu profile with inlet swirl suggests earlier boundary layer transition than with uniform inlet conditions. It should be recalled that increased turbulence intensity may account for an increase of approximately 11% in the heat transfer coefficient (an order of magnitude lower than the observed changes). Vanes n1 and n2, which are exposed to different vortices on account of the different positions in the annulus, are in reasonably good agreement.

At 50% span, there is significant augmentation on both the PS and SS with inlet swirl. On the PS Nu is increased by approximately between 50% and 200%, with the greatest changes near the leading edge region. The profiles suggest earlier transition to a fully turbulent boundary layer. High augmentation is also caused by boundary layer divergence. On the SS there is significant augmentation particularly in the leading region of the vane. This is likely caused by early transition to a turbulent boundary layer. Vanes n1 and n2 are in good agreement on the SS and in fair agreement on the PS, suggesting sensitivity to the location of the upstream vortex.

At 90% span the change in Nu with inlet swirl was minimal, although it is noted that there were limited measurements in the leading region. Examination of the surface flow (Figure 29) reveals relatively little swirl induced secondary behaviour in this region, although it is perhaps surprising that there is not a reduction in Nu on the PS at 90% span associated with the accumulation of boundary layer fluid (f) observed in Figure 18. It is possible that this effect is mitigated by higher inlet turbulence intensity.

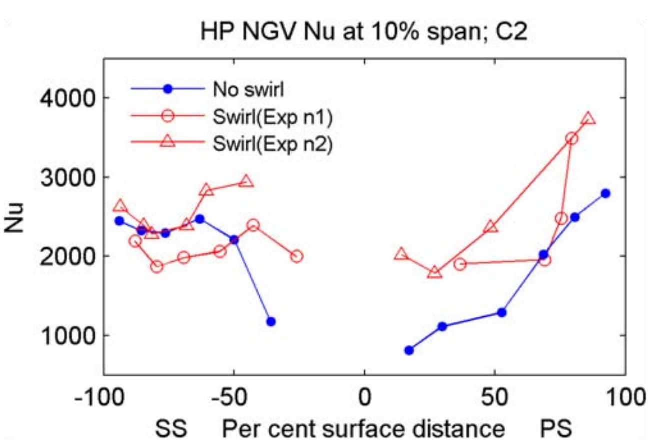

Figure 33: NGV Nu at 10% span; Uniform and Swirl-C2.

The results for the NGV in position C2 are presented in Figure 33, Figure 34 and Figure 35 for the 10, 50 and 90% span respectively. The trends with inlet swirl are similar to those for vane position C1, though less pronounced.

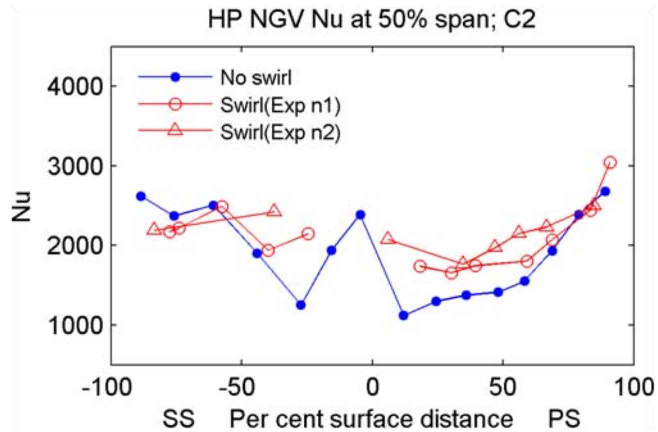

Figure 34: NGV Nu at 50% span; Uniform and Swirl-C2.

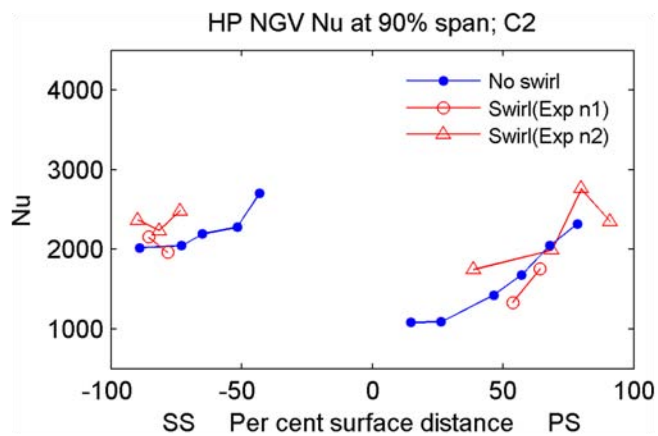

Figure 35: NGV Nu at 90% span; Uniform and Swirl-C2.

8.3 Endwall Heat Transfer Results

Heat flux measurements were performed on the hub and casing endwall of the NGV passage for uniform inlet conditions and were reduced to Nu as described in section 6.3. Competitive measurements with inlet swirl were not part of the current programme. In this section, experimental and computational results are compared for the uniform inlet condition (by way of benchmarking the CFD), and the effects due to inlet swirl are subsequently examined with reference to the computational predictions.

Figure 36(a) shows the measured Nu at the hub endwall for uniform inlet conditions. The equivalent CFD predictions are presented in Figure 36(b). The corresponding measurements and prediction on the casing are presented in Figure 37. Measured data points are shown as dots on the interpolated surface plots. Although the data are relatively sparse, the interpolated results can highlight general trends.

The overall trends in Nu distribution are similar between the experiments and CFD predictions. There is an early region of low Nu, where there is low inlet flow velocity and a relatively thick inlet boundary layer. Nu increases in the region of higher flow velocity in the downstream region of the passage and near the SS of the vane. Although the vane has minimal secondary flow, evidence of a horseshoe vortex can be seen in the CFD and experimental solutions. This is marked by a thin line of low Nu, with a region of high Nu in the PS corner of the vane where the flow reattaches with a thin boundary layer, having separated in the region of the horseshoe vortex. This effect is also described by Harvey and Jones [36].

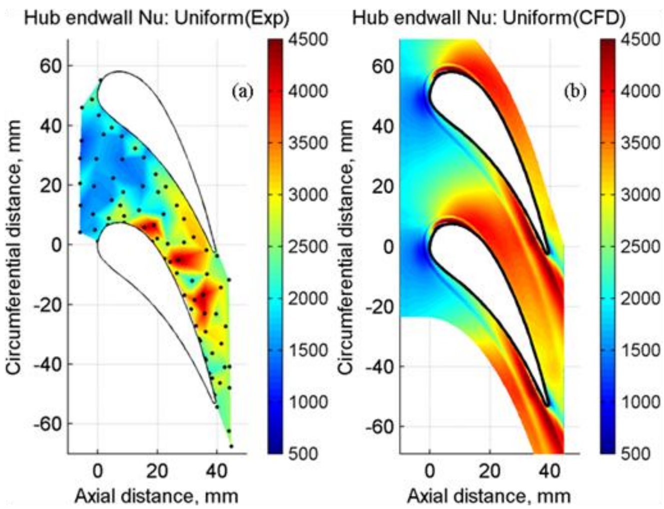

Figure 36: Hub endwall Nusselt number with Uniform inlet conditions: (a) Measured (b) Predicted.

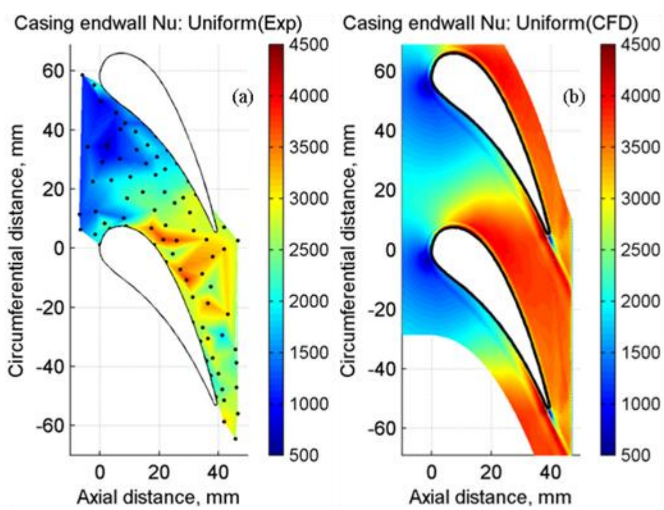

Figure 37: Casing endwall Nusselt number with Uniform inlet conditions: (a) Measured (b) Predicted.

Near the hub and casing endwall, as the flow passes beyond the point of maximum velocity (reached at approximately 80% axial chord – see Figure 12 and Figure 14), it is moderately diffused, and a reduction in Nu is seen.

The predicted surface streamline patterns on the hub and case walls are shown in Figure 38 and Figure 39 for the case of uniform inlet conditions and inlet swirl.

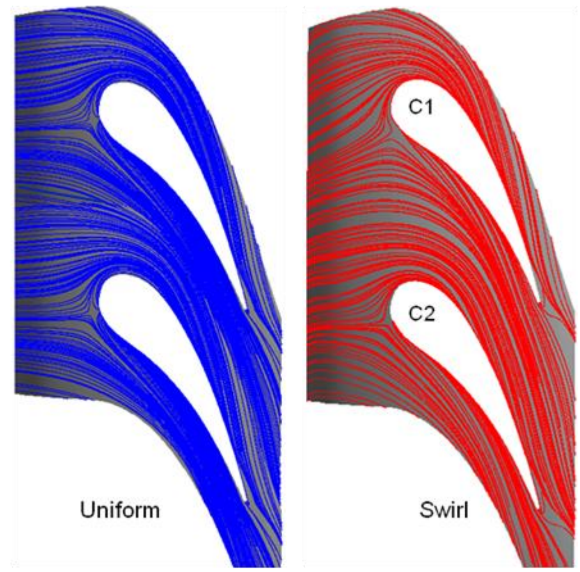

Figure 38: Predicted surface flow streamlines, with and without inlet swirl: hub endwall.

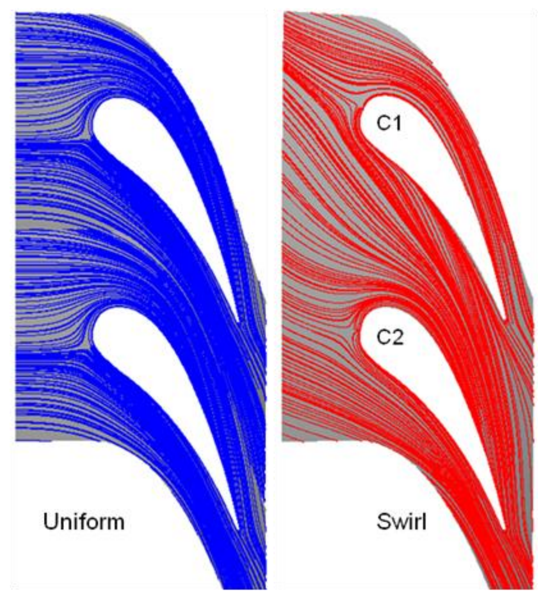

Figure 39: Predicted surface flow streamlines, with and without inlet swirl: casing endwall.

Inlet swirl acts to increase incidence at the hub and decrease incidence at the casing. On the hub endwall this causes the stagnation point to move towards the PS of the vane, increasing the loading in the section. Over-turning of the endwall boundary layer fluid is mitigated by the clockwise vortex which propagates through the passage, which offsets the effect of enhanced loading of the hub section.

On the casing endwall the effect of inlet swirl is a decrease in incidence, which lowers the loading on the vane. The strong clockwise vortex in passage C1-C2 causes greater overturning of the endwall boundary layer fluid, an effect that is less apparent in passage C2-C1.

The predicted hub endwall Nu is compared in Figure 40 for uniform inlet conditions and for inlet swirl. The averaged Nu with swirl is higher than for uniform conditions due to localised enhancement. Nu is higher by up to 25% in the region of the crown due to increased velocity, caused by higher loading. There is also enhancement in the PS TE region downstream of the horseshoe vortex lift off line. In passage C1-C2, the relatively low Nu line that marks the PS horseshoe vortex line is apparent, and appears to be enhanced due to the combination of high positive incidence on the vane and a clockwise vortex due to swirl. In passage C2-C1there is less evidence of a PS horseshoe vortex leg, and the enhancement on the SS crown is less than for passage C1-C2. This is consistent with the loading distribution on the vane shown in Figure 12 and Figure 15.

The predicted casing endwall Nu is compared in Figure 41 for uniform inlet conditions and for inlet swirl. There is a small enhancement on the SS crown of vane C1. This is not explained by an increase in surface velocities, and may be the result of reduced concentration of boundary layer fluid in the crown region (see Figure 39) causing higher momentum in the near wall region. The passage C1-C2 shows a large band of low Nu flow which suggests accumulation of boundary layer fluid in this region (see Figure 39) ahead of the PS leg of the horseshoe vortex. Behind the separation line there is a region of high Nu. Passage C2-C1 is less affected by inlet swirl.

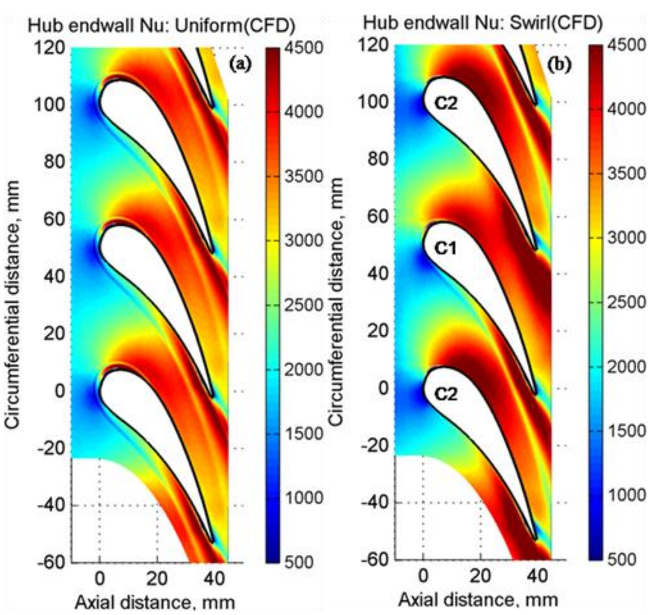

Figure 40: Predicted hub endwall Nu (a) Uniform (b) Swirl.

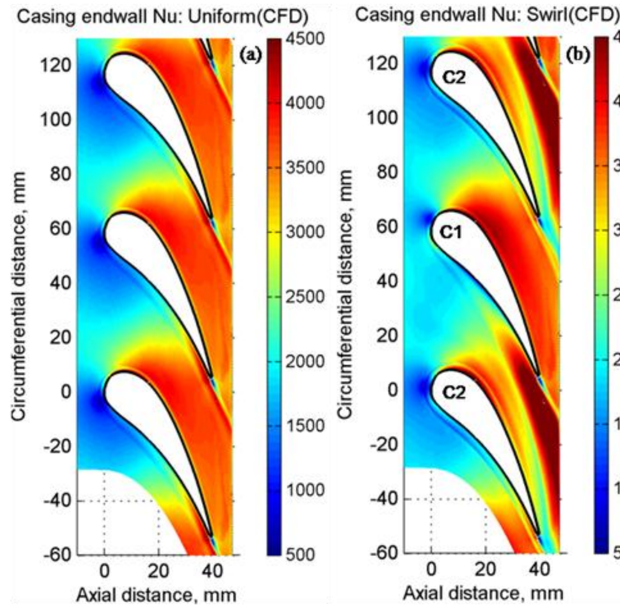

Figure 41: Predicted casing endwall Nu (a) Uniform (b) Swirl.

Circumferentially averaged Nu predictions on the hub and casing endwall are presented in Figure 42 and Figure 43 respectively, and compared to experimental data for uniform inlet conditions. On the hub endwall there is good agreement between the experimental data for uniform inlet conditions and the prediction for the same. For inlet swirl there is little effect in the leading region of the vane, but between 50% and 100% axial chord there is an enhancement in heat transfer which rises to approximately 17%.

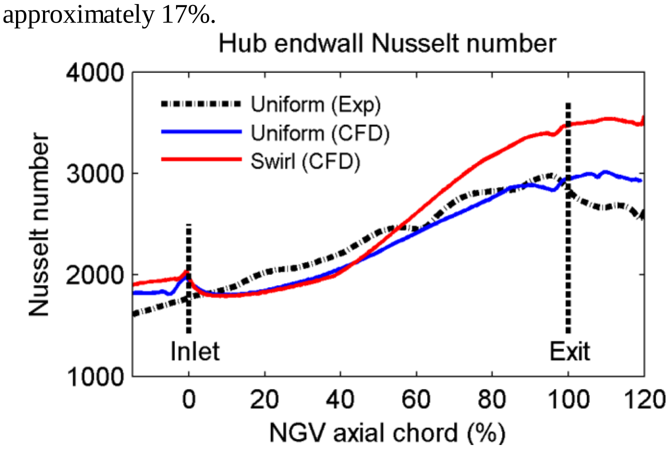

Figure 42: Hub endwall Nu; with and without inlet swirl.

On the casing endwall the agreement between the experimental data for uniform inlet conditions and the prediction for the same is less good, the former being higher by as much as 20% at approximately 50% axial chord. The predicted effect of inlet swirl is to reduce the circumferentially averaged Nu in the trailing part of the passage by up to approximately 8%.

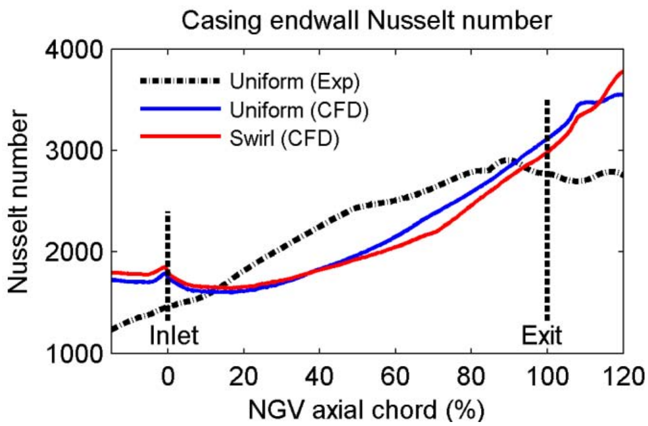

Figure 43: Casing endwall Nu; with and without inlet swirl.

9 CONCLUSIONS

A detailed experimental and computational investigation of the effect of high inlet swirl on the aerodynamic and heat transfer characteristics of a HP vane has been conducted. Experiments were performed in a rotating transonic turbine facility, which was modified to incorporate an inlet swirl generator which replicated conditions based on a low-NOx combustor design. It is believed that this is the first study of this type.

The results of the study indicate significantly altered vane loading distributions at 10% and 90% span. The stagnation point migrates towards the PS at the hub and towards the SS at the casing. The result of high positive and negative incidence at the hub and casing sections, when combined with a vortex which propagates though the vane passage, is to significantly alter the secondary flow structure of the vane. The surface flow pattern on the vane and endwall surfaces is altered such that boundary layer fluid is redistributed, causing it to collect in certain regions and dissipate in others. In the loss characteristics of the vane the effect of boundary layer fluid redistribution and altered loading characteristic is clearly evident. In particular there are loss cores associated with regions where there is streamline convergence from the vane surface flow, and regions of higher and lower loss across large regions of the span associated with higher and lower loading of the vane.

Heat transfer measurements on the vane surface demonstrate significant changes in Nu with inlet swirl. The changes are explained by streamline divergence and convergence on the surface (causing accumulation and dissipation of boundary layer fluid) and by changes in vane loading, and therefore surface velocity.

Vane endwall heat transfer predictions compared well with measurements conducted for uniform inlet conditions. Predictions for the inlet swirl condition showed significant changes in endwall Nu distribution, which can be explained with reference to the endwall secondary flow field and vane loading distribution. Higher SS crown velocities resulted in higher Nu in this region. The highest Nu values were in a region downstream of the PS leg of the horseshoe vortex, where reattachment occurs.

Perhaps the most striking observation is the extent of streamline redistribution on the PS of the vane geometrically aligned with the vortex centre. Here, extreme streamline divergence would make cooling system design challenging. The findings indicate a requirement to rethink the cooling philosophy for vanes operating in this environment.

10 NOMENCLATURE

Romans and Greeks

α	Yaw angle, degrees
β	Pitch angle, degrees
C	NGV midspan true chord, mm
ρ	Density, Kg/m^3
h	Heat transfer coefficient
k	Thermal conductivity
M	Mach number
Nu	Nusselt number
p	Pressure, bar
$\dot{q}$	Heat flux, kW/m^2
T	Temperature, K
T_{aw}	Adiabatic wall temperature, K
T_g	Gas temperature, K
T_w	Wall temperature, K
u	Velocity, m/s^2
ω	Turbine speed (rpm)

Subscripts, superscripts, abbreviations

0	Total (absolute)
1	NGV inlet plane
2	NGV exit plane
a, ax	Axial distance
rel	Rotor relative
PL	Pressure loss
Exp	Experimental
OTRF	Oxford Turbine Research Facility
TTF	Turbine Test Facility
HP	High Pressure
HTA	Heat Transfer Analogue
NGV	Nozzle Guide Vane
Tu	Turbulence
PS, SS	Pressure side, Suction side
LE, TE	Leading edge, Trailing edge
MUSCL	Monoton Upstream-centred Scheme for Conservation Laws
n1	Instrumented vane 1
n2	Instrumented vane 2
C1	Position (or vane LE) aligned with vortex centre

C2 Position (or vane LE) aligned with centre of 2 vortices

11 ACKNOWLEDGMENTS

The authors would like to acknowledge the financial support provided by the EC for the TATEF II Project, and the technical staff who supported the instrumentation and experiments at Oxford and QinetiQ Farnborough.

12 REFERENCES

[1] Gupta, A.K., Lewis, M.J., Daurer, M., 2001, "Swirl effects on combustion characteristics of premixed flames," J. Eng. Gas Turbines Power, 123, pp.619-626.

[2] Li, G., Gutmark, E.J., 2004, "Effects of swirler configurations on flow structures and combustion characteristics," ASME Paper No. GT2004-53674.

[3] Huang, Y., Yang, V., 2005, "Effects of swirl on combustion dynamics in a lean-premixed swirl-stabilized combustor," Proc. of combustion institute, 30, pp.1775-1782.

[4] Jouini, D. B. M., Sjolander, S. A., Moustapha, S. H., 2001, "Aerodynamic Performance of a Transonic Turbine Cascade at Off-Design Conditions," ASME J. Turbomachinery, Vol. 123, pp. 510-518.

[5] Corriveau, D., Sjolander, S. A., 2004, "Influence of Loading Distribution on the Performance of Transonic High Pressure Turbine Blades," ASME J. Turbomachinery, Vol. 126, pp. 288-296.

[6] Corriveau, D., Sjolander, S. A., 2007, "Influence of Loading Distribution on the Off-Design Performance of High Pressure Turbine Blades," ASME J. Turbomachinery, Vol. 129, pp. 563-571.

[7] Weiss, A. P., Fottner, L., 1995, "The Influence of Load Distribution on Secondary Flow in Straight Turbine Cascades," ASME J. Turbomachinery, Vol. 117, pp. 133-141.

[8] Benner, M. W., Sjolander, S. A., Moustapha, S. H., 2004, "The Influence of Leading-Edge Geometry on Secondary Losses in a Turbine Cascade at the Design Incidence," ASME J. Turbomachinery, Vol. 126, pp. 277-287.

[9] Goldstein, R. J., Lau, K. Y., Leung, C. C., 1983, "Velocity and Turbulence Measurements in Combustion Systems," Experiments in Fluids, 1, pp. 93-99.

[10] Hancock, P. E., Bradshaw, P., 1983, "The Effect of Freestream Turbulence on Turbulent Boundary Layers," ASME J. Fluids Engineering, Vol. 105, pp. 284-289.

[11] Blair, M. F., 1983, "Influence of Free-stream Turbulence on Turbulent Boundary Layer Heat Transfer and Men Profile Development, Part II - Analysis of Results," ASME J. Heat Transfer, Vol. 105, pp. 41-47.

[12] Krishnamoorthy, V., Sukhatme, S. P., 1989, "The Effect of Freestream Turbulence on Gas Turbine Blade Heat Transfer," ASME J. Turbomachinery, Vol. 111, pp 497-501.

[13] Ames, F. E., Wang, C., Barbot, P. A., 2003, "Measurement and Prediction of the Influence of Catalytic and Dry Low NOx Combustor Turbulence on Vane Surface Heat Transfer," ASME J. Turbomachinery, Vol. 125, pp. 221-231.

[14] Radomsky, R. W., Thole, K. A., 2002, "Detailed Boundary Layer Measurements on a Turbine Stator Vane at Elevated Freestream Turbulence Levels," ASME J. Turbomachinery, Vol. 124, pp. 107-118.

[15] Nasir, S., Carullo, J. S., Ng, W., Thole, K. A., Wu, H., Zhang, L. J., Moon, H. K., 2009, "Effects of Large Scale High Freestream Turbulence and Exit Reynolds Number on Turbine Vane Heat Transfer in a Transonic Cascade," ASME J. Turbomachinery, Vol. 131, pp. 021021-1-11.

[16] Langston, L. S., 2001, "Secondary Flows in Turbines - A Review," Annals of the New York Academy of Sciences. Vol. 934. Issue Heat Transfer in Gas Turbine Systems. pp. 11-26.

[17] Sieverding, C. H., 1985, "Secondary Flows in Straight and Annular Turbine Cascades," Thermodynamics and Fluid Mechanics of Turbo. Vol. 2 (A86- 29376 12-02). Dordrecht, Martinus Nijhoff Publishers, 1985, pp. 621-664.

[18] Yilmaz, M., Comakli, O., Yapici, S., 1999, "Enhancement of Heat Transfer by Turbulent Decaying Swirl Flow," Energy Conversion and Management; 40, pp. 1365-1376.

[19] Jacobi, A. M., Shah, R. K., 1995, "Heat Transfer Surface Enhancement through the Use of Longitudinal Vortices: A Review of Recent Progress," Experimental Thermal and Fluid Science 1995; 11, pp. 295-309.

[20] Jones, T. V., Schultz, D. L., and Hendley, A. D. 1973, "On the Flow in an Isentropic Light Piston Tunnel," MoD (Proc Exec), Aeronautical Research Council R&M No. 3731.

[21] Goodisman, M. I., Oldfield, M. L. G., Kingcombe, R. C., Jones, T. V., Ainsworth, R. W., and Brooks, A. J., 1992, "An Axial Turbobrake," ASME J. of Turbo., Vol. 114, No. 2, pp. 419–425.

[22] Hilditch, M. A., Fowler, A., Jones, T. V., Chana, K. S., Oldfield, M. L. G., Ainsworth, R. W., et al. 1994, "Installation of a Turbine Stage in the Pyestock Isentropic Light Piston Facility," ASME paper no. 94-GT-277.

[23] Povey, T., Chana, K. S., Jones, T. V., and Oldfield, M. L. G., 2003, “The Design and Performance of a Transonic Flow Deswirling System: An Application of Current CFD Design Techniques Tested Against Model and Full-Scale Experiments, Advances of CFD in Fluid Machinery Design,” IMechE Professional Engineering, pp. 65–94.

[24] Qureshi, I., Povey, T., 2011, “A Combustor-Representative Swirl Simulator for a Transonic Turbine Research Facility,” Proc. IMechE, Part G: J. Aerospace Engineering, 2011.

[25] Doorly, J. E., Oldfield, M. L. G., 1987, “The Theory of Advanced Multi-Layer Thin Film Heat Transfer Gauges,” Int. J. Heat Mass Transfer. Vol. 30, No. 6, pp. 1159-1168.

[26] Oldfield, M. L. G., 2008, “Impulse Response Processing of Transient Heat Transfer Gauge Signals,” J. of Turbo., Vol. 130, pp. 021023-1-9.

[27] Oldfield, M. L. G., Burd, H. J., Doe, N. G., 1984, “Design of Wide-Bandwidth Analogue Circuits for Heat Transfer Instrumentation in Transient Tunnels. Heat and Mass Transfer in Rotating Machinery,” (A86-24451 09-34). Washington, DC, Hemisphere Publishing Corp., 1984, pp. 233-258.

[28] Oldfield, M. L. G., Jones, T. V., Schultz, D. L., 1978, “On-Line Computer for Transient Turbine Cascade Instrumentation,” IEEE Transactions on Aerospace and Electronic Systems. Vol. AES-14, No. 5.

[29] Povey, T., 2003, "On Advances in Annular Cascade Techniques," D.Phil Thesis, Department of Engineering Science, University of Oxford.

[30] Moinier, P., and Giles, M. B., 1998, “Preconditioned Euler and Navier-Stokes Calculations on Unstructured Grids,” Proc. 6th ICFD Conference on Numerical Methods for Fluid Dynamics. Oxford, UK.

[31] Moinier, P., Mueller, J.-D., and Giles, M. B., 2001, “Edgebased Multigrid and Preconditioning for Hybrid Grids,” AIAA Journal, 40(10).

[32] Martinelli, L., 1987, “Calculations of Viscous Flows with a Multigrid Method,” PhD Thesis, Dept. of Mech. And Aerospace Eng., Princeton University, USA.

[33] Mueller, J.-D., and Giles, M. B., 1998, “Edge-Based Multigrid Schemes for Hybrid Grids,” Proc. 6th ICFD Conference on Numerical Methods for Fluid Dynamics. Oxford, UK.

[34] Chana, K. S., 1992, "Heat Transfer and Aerodynamics of a High Rim Speed Turbine Nozzle Guide Vane with Profile End Walls," ASME Paper Number 92-GT-243.

[35] Beard, P. F., 2010, "On Transient Turbine Efficiency Measurements with Engine Representative Inlet Flows," D.Phil Thesis, Department of Engineering Science, University of Oxford.

[36] Harvey, N. W., Jones, T. V., 1990, “Measurement and Calculation of Endwall Heat Transfer and Aerodynamics on a Nozzle Guide Vane in Annular Cascade,” ASME Paper No. 90-GT-301.